Research on spatial-variant property of bistatic ISAR imaging plane of space target*

Guo Bao-Feng(郭宝锋)[a)b)†], Wang Jun-Ling(王俊岭)[b)], Gao Mei-Guo(高梅国)[b)], Shang Chao-Xuan(尚朝轩)[a)], and Fu Xiong-Jun(傅雄军)[b)]

[a)] *Department of Electronic and Optical Engineering, Ordance Engineering College, Shijiazhuang* 050003, *China*
[b)] *School of Information and Electronics, Beijing Institute of Technology, Beijing* 100081, *China*

(Received 26 October 2014; revised manuscript received 11 November 2014; published online 10 February 2015)

The imaging plane of inverse synthetic aperture radar (ISAR) is the projection plane of the target. When taking an image using the range-Doppler theory, the imaging plane may have a spatial-variant property, which causes the change of scatter's projection position and results in migration through resolution cells. In this study, we focus on the spatial-variant property of the imaging plane of a three-axis-stabilized space target. The innovative contributions are as follows. 1) The target motion model in orbit is provided based on a two-body model. 2) The instantaneous imaging plane is determined by the method of vector analysis. 3) Three Euler angles are introduced to describe the spatial-variant property of the imaging plane, and the image quality is analyzed. The simulation results confirm the analysis of the spatial-variant property. The research in this study is significant for the selection of the imaging segment, and provides the evidence for the following data processing and compensation algorithm.

Keywords: space target, bistatic ISAR, imaging plane, spatial-variant property

PACS: 84.40.Xb, 91.10.Sp, 84.40.Ua **DOI:** 10.1088/1674-1056/24/4/048402

1. Introduction

Bistatic radar is a system whose transmitter and receiver are placed in different places, and the baseline length can be compared with the target distance. The operation mode makes the radar have outstanding advantages in the fight against "Four Threats".[1] Bistatic ISAR is the inverse synthetic aperture radar[2,3] system based on the bistatic radar platform. It takes imagings by receiving non-backscatter echo of the target, which can obtain more target information than monostatic radar.[4] Bistatic radar has become a research hotspot in the radar field.[5–7] Meanwhile, with the development of radar imaging technology and space technology, the imaging target is not limited to a ground target, sea target, and air target. The detection, imaging, and recognition of space targets have become a cutting-edge topic.[4,8–10]

In recent years, the research of bistatic ISAR has focused mainly on theories, which include the imaging principle, imaging resolution, imaging algorithm,[11–14] etc. The simulation and verification of the theory are mostly based on the assumption that the transmitting radar station and receiving radar station are coplanar with the target motion trajectory. Under this assumption, the ISAR imaging plane is always the bistatic plane, which refers to the plane structured by the bistatic radar and the target. Under actual conditions, the transmitting radar station and receiving radar station are generally non-coplanar with the target motion trajectory, that is, the imaging plane changes during imaging. The spatial-variant of the imaging plane will change the projection position of scatters on the target, which may result in the problem of migration through resolution cells and thus affect the image quality. Currently, there are few researches on the imaging plane and spatial-variant property. In Ref. [15], the bistatic ISAR imaging plane is determined based on the method of target rotation vector analysis, but the imaging model and signal processing model are both in the two-dimensional plane, which has some limitations. There are no references to the imaging plane spatial-variant property.

The imaging plane spatial-variant property affects the image quality. The study of the spatial-variant property can provide the evidence for the selection of the imaging orbital segment and for the following data processing and compensation algorithm. Based on this, aiming at space targets, research on the spatial-variant property of bistatic ISAR is carried out. The rest of this paper is organized as follows. In Section 2, the target motion in orbit is simulated based on the two-body model. In Section 3, a method of determining the imaging plane of a space three-axis-stabilized target is proposed. The spatial-variant property of the imaging plane is analyzed in Section 4, and the influence on image quality is given. Simulation results are shown in Section 5. Finally, some conclusions are drawn from the present study in Section 6.

*Project supported by the National Natural Science Foundation of China (Grant No. 61401024), the Shanghai Aerospace Science and Technology Innovation Foundation, China (Grant No. SAST201240), and the Basic Research Foundation of Beijing Institute of Technology (Grant No. 20140542001).

†Corresponding author. E-mail: guobao_feng870714@126.com

© 2015 Chinese Physical Society and IOP Publishing Ltd

2. Motion model of space target

Space targets generally move along the orbit. Different targets have different attitude control modes. Currently, most of the satellites adopt the three-axis-stabilized attitude control mode which has higher control precision. This paper focuses on the three-axis-stabilized space target.

The motion of a space target in orbit can be described through two-line elements (TLE). According to the given TLE, we can decide the coordinates of the target in the geocentric observation coordinate system; however, the positions of the transmitter and receiver are provided in the Earth-fixed system. So, to obtain the target's position relative to the transmitter and the receiver, we need to transfer the coordinates of radars and target into the same coordinate system. The detailed considerations are as follows. First, the coordinates of the target are transformed from the geocentric observation coordinate system to the Earth-inertial system, and then to the Earth-fixed system where radars stay. Then the coordinates are all in the Earth-fixed system, and at any time the position vectors and velocity vectors of the target relative to radars can be accurately calculated. These vectors are the premise of the imaging plane determination and spatial-variant property analysis.

In this section, the coordinate system and coordinate transformation matrix are given first, and then the target motion in orbit is simulated based on the two-body model.

2.1. Coordinate system and coordinate transformation matrix

The conceptual definitions[16] of the coordinate system in space are as follows.

(i) Geocentric equatorial coordinate system XYZ. It is also known as the Earth-inertial system. Its origin is at the center of the Earth. The X axis is aligned with the vernal equinox and the equatorial plane forms the X–Y reference plane. The Z axis points to the North Pole.

(ii) Geocentric Earth-fixed coordinate system $X'Y'Z'$. It is also known as the Earth-fixed system. Its origin is at the center of the Earth. The X' axis points to the intersection of the prime meridian with the equatorial plane. The Y' axis points to the intersection of the east longitude 90° with the equatorial plane. The Z' axis points to the North Pole. The coordinate system rotates together with the Earth.

(iii) Geocentric observation coordinate system xyz. Its origin is at the center of the Earth, the x axis points to the satellite from the geocentric. The y axis is perpendicular to the x axis in the orbital plane and points to the direction of target motion. The z axis forms the right-hand rectangular coordinate system with the x axis and y axis.

The conceptual definitions of coordinate transformation are as follows.

In a right-hand rectangular coordinate system, the rotation matrix that rotates around the X axis in the positive direction can be expressed as

$$\boldsymbol{R}_x(\theta) = \begin{bmatrix} 1 & 0 & 0 \\ 0 & \cos\theta & \sin\theta \\ 0 & -\sin\theta & \cos\theta \end{bmatrix}. \tag{1}$$

The rotation matrix that rotates around the Y axis in the positive direction can be expressed as

$$\boldsymbol{R}_y(\theta) = \begin{bmatrix} \cos\theta & 0 & -\sin\theta \\ 0 & 1 & 0 \\ \sin\theta & 0 & \cos\theta \end{bmatrix}. \tag{2}$$

The rotation matrix that rotates around the Z axis in the positive direction can be expressed as

$$\boldsymbol{R}_z(\theta) = \begin{bmatrix} \cos\theta & \sin\theta & 0 \\ -\sin\theta & \cos\theta & 0 \\ 0 & 0 & 1 \end{bmatrix}, \tag{3}$$

where, θ is the rotation angle. The definition of positive direction is the counterclockwise direction.

2.2. Orbit simulation of space target based on the two-body model

The Earth is assumed to be a sphere of uniform density distribution. Then the space target that moves around the Earth can be seen as a particle. The mass concentrates at the center of mass, equivalently. Thus, a simple two-body motion is formed as shown in Fig. 1. Under the two-body motion assumption, the orbit equation is

$$r = \frac{h^2}{\mu}\frac{1}{1+e\cos f} = a\frac{1-e^2}{1+e\cos f}, \tag{4}$$

where h is the relative angular momentum of target per unit mass, i.e., the specific relative angular momentum. Its vector form is $\boldsymbol{h} = \boldsymbol{r} \times \dot{\boldsymbol{r}}$, μ is the gravitational constant of the Earth, and its value is 3.986×10^5 km^3/s^2, $e \geq 0$ is the eccentricity, and its vector form is $\boldsymbol{e} = (\dot{\boldsymbol{r}} \times \boldsymbol{h})/\mu - \boldsymbol{r}/r$. The line defined by the vector $\boldsymbol{e}$ is commonly called the apse line, and f is the true anomaly.

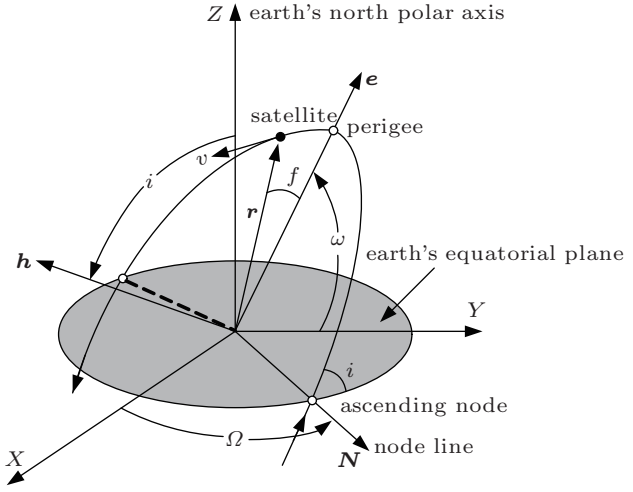


Fig. 1. Satellite orbit model.[17]

Orbit equation (4) contains three independent parameters: h, e, and f, and it describes the conic sections in the orbital plane. In the actual calculation, the angular momentum h and true anomaly f are frequently replaced by the semi-major axis a and mean anomaly M, respectively. Describing the orientation of an orbit in three dimensions requires three additional parameters, called the Euler angles, which are illustrated in Fig. 1.

First, we locate the intersection of the orbital plane with the equatorial (XY) plane. That line is called the node line. The point on the node line where the orbit passes above the equatorial plane from below it, is called the ascending node. The node line vector $\boldsymbol{N}$ extends outward from the origin through the ascending node. At the other end of the node line, where the orbit dives below the equatorial plane, is the descending node. The angle between the positive X axis and the node line is the first Euler angle Ω, the right ascension of the ascending node. The right ascension is a positive number lying between 0° and 360°.

The dihedral angle between the orbital plane and the equatorial plane is the inclination i, measured according to the right-hand rule, that is, counterclockwise around the node line vector from the equator to the orbit. The inclination is also the angle between the positive Z axis and the normal plane of the orbit. The inclination is a positive number between 0° and 180°.

The third Euler angle ω, the argument of perigee, is the angle between the node line vector $\boldsymbol{N}$ and the eccentricity vector $\boldsymbol{e}$, measured in the plane of the orbit. The argument of perigee is a positive value between 0° and 360°.

The orbit of the space target can be determined by the six orbital elements $(a,\ M,\ i,\ \omega,\ e,\ \Omega)$, where the mean anomaly can be expressed as

$$M = E - e\sin E, \tag{5}$$

with E being the eccentric anomaly, and the relationship between the eccentric anomaly and the true anomaly is

$$\tan(f/2) = \sqrt{(1+e)/(1-e)}\tan(E/2). \tag{6}$$

Considering the two-body motion, the coordinates of the target's center of mass in the geocentric observation coordinate system xyz can be expressed as

$$\left[x_S,\ y_S,\ z_S\right] = \left[r,\ 0,\ 0\right], \tag{7}$$

where r is the distance from target center to geocentre, and it can be obtained from Eq. (4).

Assuming that $\chi_{t_0} = (a,\ M_{t_0},\ i,\ \omega,\ e,\ \Omega)$ is the target's orbital element at the initial observation time, ignoring the influences of precession and nutation on the celestial pole and equinox, the coordinate system xyz can be rotated into coordinate system XYZ by a sequence of three rotations. The first step is to rotate an angle $f_{t_0}+\omega$ around the z axis clockwise. The second step is to rotate an angle i around the x axis clockwise. Finally, we clockwise-rotate around the z axis through an angle Ω. Here, f_{t_0} is the true anomaly of the initial observation time; it can be obtained by the initial orbital elements through Eqs. (5) and (6).

Except the mean anomaly, the remaining orbital elements are all constants. The mean anomaly can be obtained by

$$M_{t_0} = n(t_0 - t_{\text{epoch}}) + M_{\text{epoch}}, \tag{8}$$

where t_{epoch} is the epoch time of initial orbital elements and t_0 is the epoch time of the initial observation time.

At any observation time t, to transfer the coordinate system xyz into XYZ, the only difference relative to initial observation time t_0 is that the rotation angle around the z axis is $f_t+\omega$ rather than $f_{t_0}+\omega$, where f_t is the true anomaly of observation time t.

Therefore, the transformation matrix xyz into XYZ at the observation time t can be written as

$$\boldsymbol{R}_{x-X} = \boldsymbol{R}_z(-\Omega)\boldsymbol{R}_x(-\mathrm{i})\boldsymbol{R}_z(-f_t-\omega), \tag{9}$$

where $\boldsymbol{R}_x(\bullet)$ and $\boldsymbol{R}_z(\bullet)$ are the rotation matrices around the x axis and z axis, respectively.

Without considering the polar motion, the difference between the geocentric equatorial coordinate system XYZ and the geocentric Earth-fixed coordinate system $X'Y'Z'$ is the Earth's rotation angle (i.e., Greenwich hour angle S_{G}). Then the transformation matrix XYZ into $X'Y'Z'$ can be expressed as

$$\boldsymbol{R}_{X-X'} = \boldsymbol{R}_z(S_{G_{t_0}} + n_{\text{E}}t), \tag{10}$$

where $S_{\text{G}_{t_0}}$ is the Greenwich hour angle of the initial observation time t_0, n_{E} is the Earth's rotation angular velocity, and its period is 86164.098903691 s.

The Greenwich hour angle can be calculated from the following equation:

$$\begin{aligned} S_{\text{G}} &= 18^h.6973746 + 879000^h.0513367t_{\text{J}} \\ &\quad + 0^s.093104t_{\text{J}}^2 - 6^s.2\times10^{-6}t_{\text{J}}^3, \end{aligned} \tag{11}$$

where t_{J} can be expressed as

$$t_J = \frac{JD(t) - JD(J2000.0)}{36525.0}, \tag{12}$$

with $JD(t)$ being the Julian day at the observation time t, and $JD(J2000.0)$ the Julian day corresponding to epoch $J2000.0$.

The coordinates of the target in coordinate system $X'Y'Z'$ can be obtained by Eq. (7) through Eq. (12) together

$$\left[x_{S_X'},\ y_{S_Y'},\ z_{S_Z'}\right]^{\mathrm{T}} = \boldsymbol{R}_{X-X'}\boldsymbol{R}_{x-X}\left[x_S,\ y_S,\ z_S\right]^{\mathrm{T}}. \quad (13)$$

Assuming that the longitude, latitude, and elevation of radar are θ_{Long}, θ_{Lat}, and h_{R}, respectively, the radar coordinates in coordinate system $X'Y'Z'$ can be expressed as

$$\left[x_{\mathrm{R}},\ y_{\mathrm{R}},\ z_{\mathrm{R}}\right] = \begin{bmatrix} (R_{\mathrm{E}}+h_{\mathrm{R}})\cos\theta_{\mathrm{Lat}}\cos\theta_{\mathrm{Long}} \\ (R_{\mathrm{E}}+h_{\mathrm{R}})\cos\theta_{\mathrm{Lat}}\sin\theta_{\mathrm{Long}} \\ (R_{\mathrm{E}}+h_{\mathrm{R}})\sin\theta_{\mathrm{Lat}} \end{bmatrix}^{\mathrm{T}}, \quad (14)$$

where R_{E} is the radius of the Earth, and generally its value is 6378.15 km.

Using Eqs. (13) and (14), we can obtain the radar's observation vector relative to the target as

$$\begin{aligned} &\left[x_{\mathrm{Obs}},\ y_{\mathrm{Obs}},\ z_{\mathrm{Obs}}\right]^{\mathrm{T}} \\ &= \left[x_{S_X'},\ y_{S_Y'},\ z_{S_Z'}\right]^{\mathrm{T}} - \left[x_{\mathrm{R}},\ y_{\mathrm{R}},\ z_{\mathrm{R}}\right]^{\mathrm{T}}. \end{aligned} \quad (15)$$

For the three-axis-stabilized target, the rotation angular velocity caused by attitude stabilization of the target is equal to the true anomaly, that is, the scatter vector relative to the center of the target is constant in the observation coordinate system. Assuming that the coordinates of some scatter on target are $\left[x_i,\ y_i,\ z_i\right]^{\mathrm{T}}$ in the geocentric observation coordinate system, the coordinates in the geocentric Earth-fixed coordinate system $X'Y'Z'$ can be written as

$$\begin{aligned} \left[x_{S_i},\ y_{S_i},\ z_{S_i}\right]^{\mathrm{T}} &= \boldsymbol{R}_{X-X'}\boldsymbol{R}_{x-X}\left(\left[r,\ 0,\ 0\right]^{\mathrm{T}} + \left[x_i,\ y_i,\ z_i\right]^{\mathrm{T}}\right) \\ &= \boldsymbol{R}_z(S_{Gt_0}+n_{\mathrm{E}}t)\boldsymbol{R}_z(-\Omega)\boldsymbol{R}_x(-\mathrm{i})\boldsymbol{R}_z(-f_t-\omega)\left[r+x_i,\ y_i,\ z_i\right]^{\mathrm{T}} \\ &= \begin{bmatrix} (C_\alpha C_\gamma - S_\alpha C_\beta S_\gamma)(r+x_i)+(S_\alpha C_\gamma + C_\alpha C_\beta S_\gamma)y_i + S_\beta S_\gamma z_i \\ (-C_\alpha S_\gamma - S_\alpha C_\beta C_\gamma)(r+x_i)+(-S_\alpha S_\gamma + C_\alpha C_\beta C_\gamma)y_i + S_\beta C_\gamma z_i \\ S_\alpha S_\beta (r+x_i) - (C_\alpha S_\beta)y_i + C_\beta z_i \end{bmatrix}, \end{aligned} \quad (16)$$

where C_α and S_α represent the sine and cosine function of angle α respectively. In the above formula, $\alpha = -f_t - \omega$, $\beta = -\mathrm{i}$, and $\gamma = -(-S_{Gt_0} - n_{\mathrm{E}}t + \Omega)$.

The scatter's position vector relative to radar is

$$\begin{aligned} &\left[x_{\mathrm{Obs}_i},\ y_{\mathrm{Obs}_i},\ z_{\mathrm{Obs}_i}\right]^{\mathrm{T}} = \left[x_{S_i},\ y_{S_i},\ z_{S_i}\right]^{\mathrm{T}} - \left[x_{\mathrm{R}},\ y_{\mathrm{R}},\ z_{\mathrm{R}}\right]^{\mathrm{T}} \\ &= \begin{bmatrix} (C_\alpha C_\gamma - S_\alpha C_\beta S_\gamma)(r+x_i)+(S_\alpha C_\gamma + C_\alpha C_\beta S_\gamma)y_i + S_\beta S_\gamma z_i \\ (-C_\alpha S_\gamma - S_\alpha C_\beta C_\gamma)(r+x_i)+(-S_\alpha S_\gamma + C_\alpha C_\beta C_\gamma)y_i + S_\beta C_\gamma z_i \\ S_\alpha S_\beta (r+x_i) - (C_\alpha S_\beta)y_i + C_\beta z_i \end{bmatrix} - \begin{bmatrix} (R_{\mathrm{E}}+h_{\mathrm{R}})\cos\theta_{\mathrm{Lat}}\cos\theta_{\mathrm{Long}} \\ (R_{\mathrm{E}}+h_{\mathrm{R}})\cos\theta_{\mathrm{Lat}}\sin\theta_{\mathrm{Long}} \\ (R_{\mathrm{E}}+h_{\mathrm{R}})\sin\theta_{\mathrm{Lat}} \end{bmatrix}. \end{aligned} \quad (17)$$

From Eq. (17), we can obtain the distance from radar to the scatter as follows:

$$r_{\mathrm{Dis}_i} = \sqrt{x_{\mathrm{Obs}_i}^2 + y_{\mathrm{Obs}_i}^2 + z_{\mathrm{Obs}_i}^2}\,. \quad (18)$$

We take the first and second derivatives of Eq. (18) to obtain the radial velocity and acceleration:

$$\dot{r}_{\mathrm{Dis}_i} = \frac{x_{\mathrm{Obs}_i}\dot{x}_{\mathrm{Obs}_i} + y_{\mathrm{Obs}_i}\dot{y}_{\mathrm{Obs}_i} + z_{\mathrm{Obs}_i}\dot{z}_{\mathrm{Obs}_i}}{\sqrt{x_{\mathrm{Obs}_i}^2 + y_{\mathrm{Obs}_i}^2 + z_{\mathrm{Obs}_i}^2}}, \quad (19)$$

$$\ddot{r}_{\mathrm{Dis}_i} = \frac{\dot{x}_{\mathrm{Obs}_i}^2 + \ddot{x}_{\mathrm{Obs}_i}\dot{x}_{\mathrm{Obs}_i} + \dot{y}_{\mathrm{Obs}_i}^2 + y_{\mathrm{Obs}_i}\ddot{y}_{\mathrm{Obs}_i} + \dot{z}_{\mathrm{Obs}_i}^2 + z_{\mathrm{Obs}_i}\ddot{z}_{\mathrm{Obs}_i}}{\sqrt{x_{\mathrm{Obs}_i}^2 + y_{\mathrm{Obs}_i}^2 + z_{\mathrm{Obs}_i}^2}} - \frac{(x_{\mathrm{Obs}_i}\dot{x}_{\mathrm{Obs}_i} + y_{\mathrm{Obs}_i}\dot{y}_{\mathrm{Obs}_i} + z_{\mathrm{Obs}_i}\dot{z}_{\mathrm{Obs}_i})^2}{(\sqrt{x_{\mathrm{Obs}_i}^2 + y_{\mathrm{Obs}_i}^2 + z_{\mathrm{Obs}_i}^2})^3}, \quad (20)$$

where $\dot{x}$ and $\ddot{x}$ respectively represent the first and second derivatives of x, and they can be obtained from Eq. (17).

Through the orbit simulation based on the two-body model, we can obtain the position of the target from Eq. (16) and also obtain the radar position from Eq. (14) in the geocentric Earth-fixed coordinate system $X'Y'Z'$ at any time. Bistatic ISAR consists of two radars placed at different places, and the scatter's position vector and other parameters (radial velocity, acceleration, and so on) relative to either radar can be obtained.

3. Imaging plane determination in space

The imaging plane is the projection plane of ISAR. The change of imaging plane during imaging forms the spatial-variant property. This section focuses on the determination method the imaging plane. Since the space turntable imaging model is for a special case of ISAR, the imaging plane determination method is studied aiming first at the turntable model and then at the space three-axis-stabilized target.

3.1. Bistatic ISAR imaging plane determination of turntable model

Figure 2 illustrates the topology of bistatic ISAR imaging plane, where *oxyz* is the right-hand coordinate system with its origin *o* located at the target's center, and the *x* axis points to the transmitter. The *y* axis lying in the bistatic plane is perpendicular to the *x* axis. The *z* axis forms a right-hand rectangular coordinate system with the *x* axis and *y* axis. $\hat{\boldsymbol{R}}_{\mathrm{T}}$ and $\hat{\boldsymbol{R}}_{\mathrm{R}}$ denote the target's line of sight (LOS) unit vectors pointing to the transmitter and receiver respectively. The target rotates around *o*, and its effective rotation vector is $\boldsymbol{\omega}_{\Sigma}$.

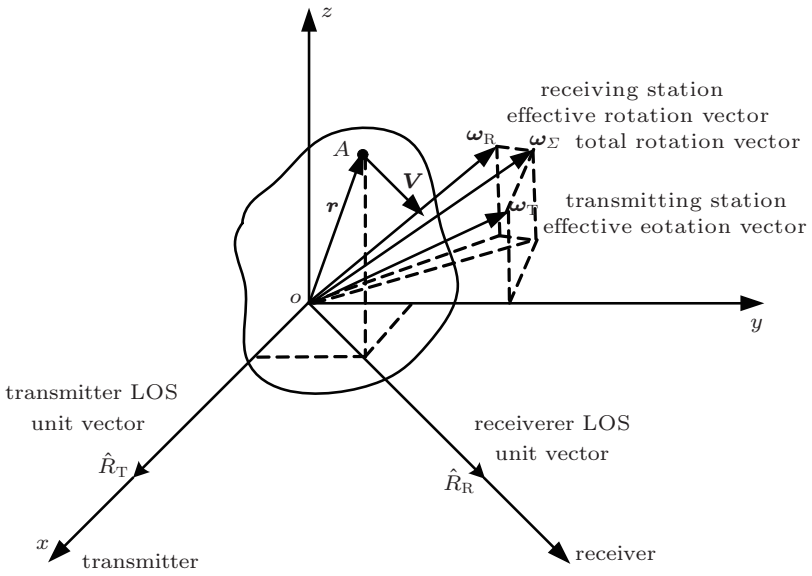


Fig. 2. General topology of bistatic ISAR imaging plane.

For some scatter *A* on the target, its position vector is *r*, then the velocity *V* of scatter *A* caused by target rotation can be expressed as

$$\boldsymbol{V} = \boldsymbol{r} \times \boldsymbol{\omega}_{\Sigma}. \tag{21}$$

Note that the bistatic Doppler frequency is the summation of the Doppler frequency created by the velocity vector respectively on the transmitter LOS and receiver LOS. Then the instantaneous rotation bistatic Doppler frequency of scatter *A* could be given as

$$f_{\mathrm{d}} = -\frac{f_{\mathrm{c}}}{c}\left(V \cdot \hat{\boldsymbol{R}}_{\mathrm{T}} + V \cdot \hat{\boldsymbol{R}}_{\mathrm{R}}\right) \tag{22}$$

Substituting Eq. (21) into Eq. (22) leads to

$$\begin{aligned} f_{\mathrm{d}} &= -\frac{f_{\mathrm{c}}}{c}\left[(r \times \boldsymbol{\omega}_{\Sigma}) \cdot \hat{\boldsymbol{R}}_{\mathrm{T}} + (r \times \boldsymbol{\omega}_{\Sigma}) \cdot \hat{\boldsymbol{R}}_{\mathrm{R}}\right] \\ &= \frac{f_{\mathrm{c}}}{c} r \cdot \left(\hat{\boldsymbol{R}}_{\mathrm{T}} \times \boldsymbol{\omega}_{\Sigma} + \hat{\boldsymbol{R}}_{\mathrm{R}} \times \boldsymbol{\omega}_{\Sigma}\right). \end{aligned} \tag{23}$$

Let $\boldsymbol{\omega}_{\mathrm{T}}$ represent the projection vector of $\boldsymbol{\omega}_{\Sigma}$ on the plane perpendicular to $\hat{\boldsymbol{R}}_{\mathrm{T}}$, and $\boldsymbol{\omega}_{\mathrm{R}}$ denotes the projection vector of $\boldsymbol{\omega}_{\Sigma}$ on the plane perpendicular to $\hat{\boldsymbol{R}}_{\mathrm{R}}$, then we will have

$$\hat{\boldsymbol{R}}_{\mathrm{T}} \times \boldsymbol{\omega}_{\Sigma} = \hat{\boldsymbol{R}}_{\mathrm{T}} \times \boldsymbol{\omega}_{\mathrm{T}}, \hat{\boldsymbol{R}}_{\mathrm{R}} \times \boldsymbol{\omega}_{\Sigma} = \hat{\boldsymbol{R}}_{\mathrm{R}} \times \boldsymbol{\omega}_{\mathrm{R}}. \tag{24}$$

Substituting Eq. (24) into Eq. (23) yields

$$f_{\mathrm{d}} = \frac{f_{\mathrm{c}}}{c} \boldsymbol{r} \cdot \left(\hat{\boldsymbol{R}}_{\mathrm{T}} \times \boldsymbol{\omega}_{\mathrm{T}} + \hat{\boldsymbol{R}}_{\mathrm{R}} \times \boldsymbol{\omega}_{\mathrm{R}}\right). \tag{25}$$

We can see that the bistatic Doppler frequency is the projection of position vector $\boldsymbol{r}$ on vector $\left(\hat{\boldsymbol{R}}_{\mathrm{T}} \times \boldsymbol{\omega}_{\mathrm{T}} + \hat{\boldsymbol{R}}_{\mathrm{R}} \times \boldsymbol{\omega}_{\mathrm{R}}\right)$, that is, $\left(\hat{\boldsymbol{R}}_{\mathrm{T}} \times \boldsymbol{\omega}_{\mathrm{T}} + \hat{\boldsymbol{R}}_{\mathrm{R}} \times \boldsymbol{\omega}_{\mathrm{R}}\right)$ is the cross range direction. As is well known, the range direction is the gradient vector of an equidistant surface. Since the equidistant surface of bistatic radar is of an ellipse whose foci are at the transmitter and receiver respectively, its gradient vector direction is the direction of bistatic angle bisector, i.e., the direction of vector $\left(\hat{\boldsymbol{R}}_{\mathrm{T}} + \hat{\boldsymbol{R}}_{\mathrm{R}}\right)$.

Thus, the range direction of bistatic ISAR is determined by

$$\boldsymbol{\Theta} = \hat{\boldsymbol{R}}_{\mathrm{T}} + \hat{\boldsymbol{R}}_{\mathrm{R}}, \tag{26}$$

and the cross range direction of bistatic ISAR is determined by

$$\boldsymbol{\Xi} = \hat{\boldsymbol{R}}_{\mathrm{T}} \times \boldsymbol{\omega}_{\mathrm{T}} + \hat{\boldsymbol{R}}_{\mathrm{R}} \times \boldsymbol{\omega}_{\mathrm{R}}. \tag{27}$$

Vectors $\boldsymbol{\Theta}$ and $\boldsymbol{\Xi}$ determine the imaging plane, and the signs of vectors $\boldsymbol{\Theta}$ and $\boldsymbol{\Xi}$ have no effect on the imaging plane determination. We can also see that the vector $\boldsymbol{\Theta}$ is always perpendicular to $\boldsymbol{\Xi}$ in the case of the turntable model.

3.2. Bistatic ISAR imaging plane determination of space three-axis-stabilized target

The motion forms of the space three-axis-stabilized target include the translational motion and the rotation around the target center of mass. The translational motion of the target

will cause the change of visual angle, which can also provide the bistatic Doppler frequency. Thus, the cross range direction is determined by both the translational motion and the rotation.

Assume that the translational motion velocity is $\boldsymbol{v}$. Note that $\boldsymbol{v}$ here is different from the rotation velocity $\boldsymbol{V}$. We know that the radial velocity relative to transmitter and receiver cannot cause the visual angle to change. Let v_{T} represent the projection vector of v on the plane perpendicular to $\hat{\boldsymbol{R}}_{\mathrm{T}}$, and $\boldsymbol{v}_{\mathrm{R}}$ denote the projection vector of $\boldsymbol{v}$ on the plane perpendicular to $\hat{\boldsymbol{R}}_{\mathrm{R}}$, then we will have

$$\boldsymbol{v}\times\hat{\boldsymbol{R}}_{\mathrm{T}}=v_{\mathrm{T}}\times\hat{\boldsymbol{R}}_{\mathrm{T}},\quad \boldsymbol{v}\times\hat{\boldsymbol{R}}_{\mathrm{R}}=v_{\mathrm{R}}\times\hat{\boldsymbol{R}}_{\mathrm{R}}. \tag{28}$$

Then the total rotation vector consists of two parts, one is caused by the translational motion and the other by attitude-stabilized rotation. Let $\boldsymbol{\omega}_{v\mathrm{T}}$ and $\boldsymbol{\omega}_{v\mathrm{R}}$ be the rotation vectors caused by translational motion relative to transmitter and receiver respectively, then they will be expressed respectively as

$$\begin{aligned}\boldsymbol{\omega}_{v\mathrm{T}}&=\frac{\boldsymbol{v}\times\hat{\boldsymbol{R}}_{\mathrm{T}}}{R_{\mathrm{T}}}=\frac{\boldsymbol{v}_{\mathrm{T}}\times\hat{\boldsymbol{R}}_{\mathrm{T}}}{R_{\mathrm{T}}},\\ \boldsymbol{\omega}_{v\mathrm{R}}&=\frac{\boldsymbol{v}\times\hat{\boldsymbol{R}}_{\mathrm{R}}}{R_{\mathrm{R}}}=\frac{\boldsymbol{v}_{\mathrm{R}}\times\hat{\boldsymbol{R}}_{\mathrm{R}}}{R_{\mathrm{R}}},\end{aligned} \tag{29}$$

where R_{T} and R_{R} are the distances from the center of target to transmitter and to receiver, respectively. Assuming that the attitude-stabilized rotation vector is $\boldsymbol{\omega}_{\mathrm{s}}$, and $\boldsymbol{\omega}_{\mathrm{sT}}$ is the projection of $\boldsymbol{\omega}_{\mathrm{s}}$ on the plane perpendicular to $\hat{\boldsymbol{R}}_{\mathrm{T}}$, $\boldsymbol{\omega}_{\mathrm{sR}}$ is the projection of $\boldsymbol{\omega}_{\mathrm{s}}$ on the plane perpendicular to $\hat{\boldsymbol{R}}_{\mathrm{R}}$, then

$$\hat{\boldsymbol{R}}_{\mathrm{T}}\times\boldsymbol{\omega}_{\mathrm{s}}=\hat{\boldsymbol{R}}_{\mathrm{T}}\times\boldsymbol{\omega}_{\mathrm{sT}},\quad \hat{\boldsymbol{R}}_{\mathrm{R}}\times\boldsymbol{\omega}_{\mathrm{s}}=\hat{\boldsymbol{R}}_{\mathrm{R}}\times\boldsymbol{\omega}_{\mathrm{sR}}. \tag{30}$$

The total rotation vectors $\boldsymbol{\omega}_{\Sigma\mathrm{T}}$ and $\boldsymbol{\omega}_{\Sigma\mathrm{R}}$ of the target relative to transmitter and receiver can be written as

$$\boldsymbol{\omega}_{\Sigma\mathrm{T}}=\boldsymbol{\omega}_{\mathrm{sT}}+\boldsymbol{\omega}_{v\mathrm{T}},\quad \boldsymbol{\omega}_{\Sigma\mathrm{R}}=\boldsymbol{\omega}_{\mathrm{sR}}+\boldsymbol{\omega}_{v\mathrm{R}}. \tag{31}$$

Substituting Eqs. (29)–(31) into Eq. (27), we obtain the cross range direction of bistatic ISAR of three-axis-stabilized target.

$$\begin{aligned}\boldsymbol{\Xi}&=\hat{\boldsymbol{R}}_{\mathrm{T}}\times\boldsymbol{\omega}_{\Sigma\mathrm{T}}+\hat{\boldsymbol{R}}_{\mathrm{R}}\times\boldsymbol{\omega}_{\Sigma\mathrm{R}}\\ &=\hat{\boldsymbol{R}}_{\mathrm{T}}\times(\boldsymbol{\omega}_{\mathrm{sT}}+\boldsymbol{\omega}_{v\mathrm{T}})+\hat{\boldsymbol{R}}_{\mathrm{R}}\times(\boldsymbol{\omega}_{\mathrm{sR}}+\boldsymbol{\omega}_{v\mathrm{R}})\\ &=\hat{\boldsymbol{R}}_{\mathrm{T}}\times\left(\boldsymbol{\omega}_{\mathrm{sT}}+\frac{\boldsymbol{v}_{\mathrm{T}}\times\hat{\boldsymbol{R}}_{\mathrm{T}}}{R_{\mathrm{T}}}\right)+\hat{\boldsymbol{R}}_{\mathrm{R}}\\ &\quad\times\left(\boldsymbol{\omega}_{\mathrm{sR}}+\frac{\boldsymbol{v}_{\mathrm{R}}\times\hat{\boldsymbol{R}}_{\mathrm{R}}}{R_{\mathrm{R}}}\right).\end{aligned} \tag{32}$$

According to vector product formula $\boldsymbol{a}\times\boldsymbol{b}\times\boldsymbol{c}=(\boldsymbol{a}\cdot\boldsymbol{c})\,\boldsymbol{b}-(\boldsymbol{b}\cdot\boldsymbol{c})\,\boldsymbol{a}$, we can obtain that

$$\hat{\boldsymbol{R}}_{\mathrm{T}}\times\boldsymbol{v}_{\mathrm{T}}\times\hat{\boldsymbol{R}}_{\mathrm{T}}=\left(\hat{\boldsymbol{R}}_{\mathrm{T}}\cdot\hat{\boldsymbol{R}}_{\mathrm{T}}\right)\boldsymbol{v}_{\mathrm{T}}-\left(\boldsymbol{v}_{\mathrm{T}}\cdot\hat{\boldsymbol{R}}_{\mathrm{T}}\right)\hat{\boldsymbol{R}}_{\mathrm{T}}=\boldsymbol{v}_{\mathrm{T}}, \tag{33}$$

$$\hat{\boldsymbol{R}}_{\mathrm{R}}\times\boldsymbol{v}_{\mathrm{R}}\times\hat{\boldsymbol{R}}_{\mathrm{R}}=\left(\hat{\boldsymbol{R}}_{\mathrm{R}}\cdot\hat{\boldsymbol{R}}_{\mathrm{R}}\right)\boldsymbol{v}_{\mathrm{R}}-\left(\boldsymbol{v}_{\mathrm{R}}\cdot\hat{\boldsymbol{R}}_{\mathrm{R}}\right)\hat{\boldsymbol{R}}_{\mathrm{R}}=\boldsymbol{v}_{\mathrm{R}}. \tag{34}$$

Substituting Eqs. (33) and (34) into Eq. (32) yields

$$\boldsymbol{\Xi}=\left(\hat{\boldsymbol{R}}_{\mathrm{T}}\times\boldsymbol{\omega}_{\mathrm{sT}}+\hat{\boldsymbol{R}}_{\mathrm{R}}\times\boldsymbol{\omega}_{\mathrm{sR}}\right)+\left(\frac{\boldsymbol{v}_{\mathrm{T}}}{R_{\mathrm{T}}}+\frac{\boldsymbol{v}_{\mathrm{R}}}{R_{\mathrm{R}}}\right). \tag{35}$$

Let

$$\boldsymbol{\Xi}_1=\hat{\boldsymbol{R}}_{\mathrm{T}}\times\boldsymbol{\omega}_{\mathrm{sT}}+\hat{\boldsymbol{R}}_{\mathrm{R}}\times\boldsymbol{\omega}_{\mathrm{sR}}$$

and

$$\boldsymbol{\Xi}_2=\boldsymbol{v}_{\mathrm{T}}/R_{\mathrm{T}}+\boldsymbol{v}_{\mathrm{R}}/R_{\mathrm{R}},$$

then $\boldsymbol{\Xi}_1$ which is similar to Eq. (27) will be a cross range vector caused by attitude-stabilized rotation, and $\boldsymbol{\Xi}_2$ is the cross range vector caused by the translational motion of target.

The bistatic ISAR range direction of the three-axis-stabilized target is also the direction of bistatic angle bisector, and it can be written as

$$\boldsymbol{\Theta}=\hat{\boldsymbol{R}}_{\mathrm{T}}+\hat{\boldsymbol{R}}_{\mathrm{R}}. \tag{36}$$

Note that the vector $\boldsymbol{\Theta}$ is not always perpendicular to vector $\boldsymbol{\Xi}$.

The space target can be regarded as the cooperative target, and we can obtain its position vector and velocity vector at any time through the six orbital elements. Then the cross range direction $\boldsymbol{\Xi}$ and range direction $\boldsymbol{\Theta}$ can be obtained according to Eqs. (35) and (36). $\boldsymbol{\Theta}$ and $\boldsymbol{\Xi}$ together determine the imaging plane.

4. Spatial-variant property analysis of imaging plane

ISAR is a powerful signal processing technique for imaging moving targets in range-Doppler domains. The required range resolution is achieved by using the finite frequency bandwidth of the transmitted signal, and the cross range resolution by different look angles and Doppler histories.

The spatial-variant property of the imaging plane causes the change of scatters' projection position onto the imaging plane. When the spatial-variant property is serious, the phenomenon of migration through resolution cells occurs, which results in image blurring.

The purpose of spatial-variant property analysis is to find the scatters' range histories projected onto the range axis, which provides the evidence of image quality analysis. If the position change projected onto the range axis does not exceed a range resolution cell, it will not cause the migration through range cells, and we can determine whether the migration through Doppler cells exists by the scatters' Doppler histories.

First, in this section the spatial-variant property of the space three-axis-stabilized target is analyzed. Then the range histories and Doppler histories of scatters are obtained in the case of spatial-variant. Finally, the image quality is analyzed.

4.1. Spatial-variant property analysis of the imaging plane of three-axis-stabilized target

When the imaging plane is spatial-variant, the geometry of bistatic ISAR is shown in Fig. 3, where T is the transmitter, R is the receiver, and L denotes the length of the baseline of bistatic ISAR. At the imaging initial time t_1, a right-hand coordinate system $x_1y_1z_1$ is established. Its origin O_1 is at the center of the target, the y_1 axis is the range axis, i.e., the bistatic angle bisector direction. The x_1 axis is perpendicular to the y_1 axis in the bistatic plane, and the z_1 axis is perpendicular to the $x_1O_1y_1$ plane. P is a scatter on the target, at the time t_1, we denote it as P_1, and its coordinates are (x_P, y_P, z_p) in the $x_1y_1z_1$ system. At the imaging time t_m, O_m is the center of the target and we write the scatter P as P_m. Based on this, a right-hand coordinate system $x_my_mz_m$ is established with O_m representing its origin, the y_m axis pointing to the bistatic angle bisector direction, the x_m axis being perpendicular to the y_m axis in the bistatic plane, and the z_m axis perpendicular to the $x_mO_my_m$ plane. In the coordinate system $x_my_mz_m$, the coordinates of scatter P_m are (x_{Pm}, y_{Pm}, z_{pm}). At the times t_1 and t_m, the bistatic angles are β_1 and β_m, and the intersections of the bistatic angle bisector with the baseline are Q_1 and Q_m, respectively.

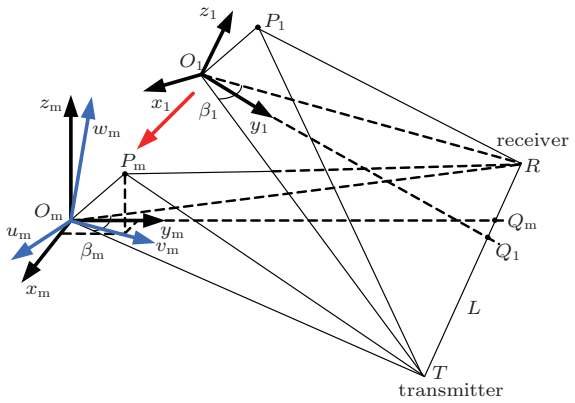


Fig. 3. (color online) Geometry of bistatic ISAR.

The space three-axis-stabilized target also rotates while it has the translational motion component. The rotation causes the change of the scatter projection position as well as the translational motion. The rotation axis goes through the center of the target and it is parallel to the normal line of the orbital plane. During imaging, the rotation axis and rotation angular velocity can be regarded as constants. The process that the target rotates around the rotation axis is equivalent to that the target stays stationary (i.e., translational motion only) and the radars rotate around the rotation axis inversely along with the coordinate system. After the rotation of radars and the coordinate system, a new coordinate system is obtained. The scatters' coordinate values in the new coordinate system reflect not only the different look angles but also the target's attitude-stabilized rotation. From the coordinate values we can obtain the range histories of any scatter, and the Doppler frequency can be easily found by taking the slow time derivative of range histories.

Assuming that the attitude-stabilized rotation unit vector of the target is $\boldsymbol{A}(A_x, A_y, A_z)$. From t_1 to t_m, the rotation angle is $-\eta_m$. Note that the minus sign represents the clockwise rotation. Then counterclockwise rotating the space coordinate system $x_my_mz_m$ around rotation axis $\boldsymbol{A}$ through the angle η_m, we can obtain a new coordinate system $u_mv_mw_m$, and it implies the attitude-stabilized rotation of the target. Let $\hat{\boldsymbol{x}}_1$, $\hat{\boldsymbol{y}}_1$, $\hat{\boldsymbol{z}}_1$ be the three axis unit vectors of coordinate system $x_1y_1z_1$, $\hat{\boldsymbol{x}}_m$, $\hat{\boldsymbol{y}}_m$, $\hat{\boldsymbol{z}}_m$ be the three axis unit vectors of coordinate system $x_my_mz_m$, $\hat{\boldsymbol{u}}_m$, $\hat{\boldsymbol{v}}_m$, $\hat{\boldsymbol{w}}_m$ be the three axis unit vectors of coordinate system $u_mv_mw_m$. All the unit vectors are row vectors of 1×3 in size. Since $u_mv_mw_m$ is obtained from $x_my_mz_m$, according to Eqs. (A18) and (A19) in Appendix A, we can obtain that

$$\begin{bmatrix} \hat{\boldsymbol{u}}_m \\ \hat{\boldsymbol{v}}_m \\ \hat{\boldsymbol{w}}_m \end{bmatrix} = \begin{bmatrix} \hat{\boldsymbol{x}}_m \\ \hat{\boldsymbol{y}}_m \\ \hat{\boldsymbol{z}}_m \end{bmatrix} \cdot \boldsymbol{R}_{\mathrm{S}}(\eta_m). \tag{37}$$

The transformation matrix $R_{\mathrm{s}}(\eta_m)$ is derived in Appendix A.

Since the coordinates of scatter P_1 are (x_p, y_p, z_p) in the $x_1y_1z_1$ system, to obtain the coordinates of P_m in $u_mv_mw_m$, it is necessary to deduce the transformation relationship between $x_1y_1z_1$ and $u_mv_mw_m$. As is well known, any two rectangular coordinate systems in space can be mutually transformed by a sequence of three rotations and a shift of the origin, which is illustrated in Fig. 4. Three rotations are the Euler angles, i.e., yaw angle, pitch angle, and roll angle. We define that the yaw angle is the angle rotating around the z axis, the pitch angle is the angle rotating around the y axis, and the roll angle is the angle rotating around the x axis. The shift of the origin has no influence on the directions of coordinate axes. Without considering the origin position, to transfer the $x_1y_1z_1$ system into the $u_mv_mw_m$ system, we need three rotations.

The first step is to rotate the $x_1o_1y_1$ through a yaw angle φ_{zm} around the z_1 axis. Then we obtain a new coordinate system $x_1'y_1'z_1'$, and the directions of the z_1' axis and z_1 axis are the same. We can obtain the orthogonal transformation matrix $\boldsymbol{R}_z(\varphi_{zm})$ by Eq. (3).

The second step is to rotate the $x_1'o_1z_1'$ through a pitch angle φ_{ym} around the y_1' axis. Then we obtain a new coordinate system $x_1''y_1''z_1''$, and the directions of the y_1'' axis and y_1' axis are the same. We can obtain the orthogonal transformation matrix $\boldsymbol{R}_y(\varphi_{ym})$ by Eq. (2).

The third step, i.e., the last step is to rotate the $x_1''y_1''z_1''$ through a roll angle φ_{xm} around the x_1'' axis. Then we obtain a new coordinate system $x_1'''y_1'''z_1'''$, and the directions of the x_1''' axis and x_1'' axis are the same. We can obtain the orthogonal transformation matrix $\boldsymbol{R}_x(\varphi_{xm})$ by Eq. (1).

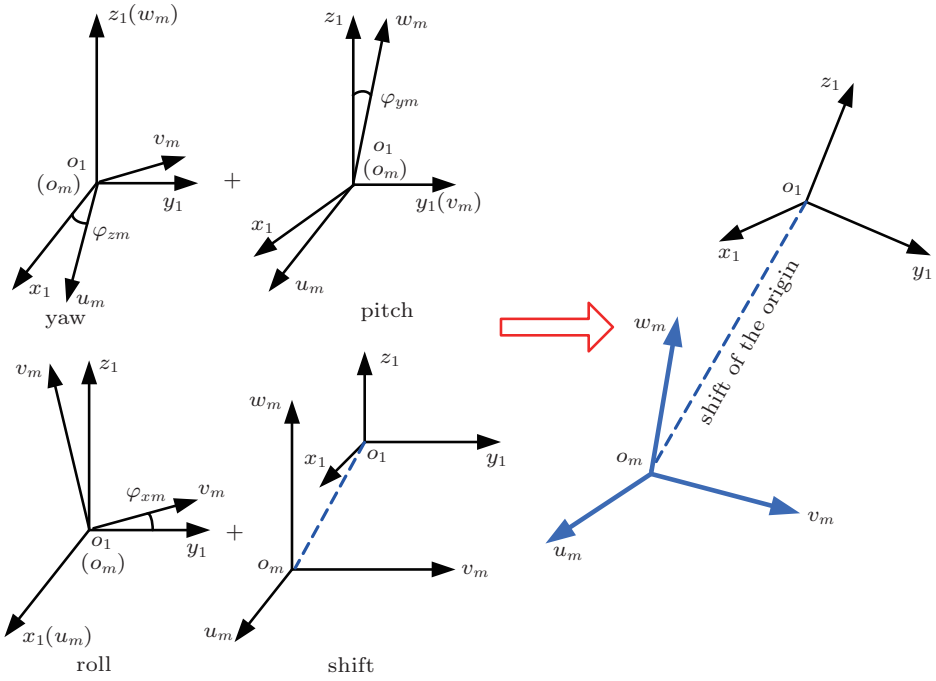


Fig. 4. (color online) Schematic diagram of coordinate transformation in space.

There always exists a set of Euler angles φ_{zm}, φ_{ym}, and φ_{xm} so that the directions of $x_1'''y_1'''z_1'''$ and $u_mv_mw_m$ are totally the same. Let ξ_{zm}, ξ_{ym} and ξ_{xm} be the Euler angles satisfying this condition. Then the transformation matrix transferring the $x_1y_1z_1$ system into the $u_mv_mw_m$ system is the product of the three matrices obtained above, i.e.,

$$\begin{aligned}\boldsymbol{R}_{\boldsymbol{xyz_m}} &= \boldsymbol{R}_{\boldsymbol{x}}(\xi_{xm})\,\boldsymbol{R}_{\boldsymbol{y}}(\xi_{ym})\,\boldsymbol{R}_{\boldsymbol{z}}(\xi_{zm}) \\ &= \begin{bmatrix} \cos\xi_{zm}\cos\xi_{ym} & \sin\xi_{zm}\cos\xi_{ym} & -\sin\xi_{ym} \\ -\sin\xi_{zm}\cos\xi_{xm}+ \\ \cos\xi_{zm}\sin\xi_{ym}\sin\xi_{xm} & \cos\xi_{zm}\cos\xi_{xm}+ \\ & \sin\xi_{zm}\sin\xi_{ym}\sin\xi_{xm} & \cos\xi_{ym}\sin\xi_{xm} \\ \sin\xi_{zm}\sin\xi_{xm}+ \\ \cos\xi_{zm}\sin\xi_{ym}\cos\xi_{xm} & -\cos\xi_{zm}\sin\xi_{xm}+ \\ & \sin\xi_{zm}\sin\xi_{ym}\cos\xi_{xm} & \cos\xi_{ym}\cos\xi_{xm} \end{bmatrix}. \end{aligned} \tag{38}$$

Then the axial directions of $u_mv_mw_m$ and $x_1y_1z_1$ satisfy the following equation:

$$\begin{bmatrix} \hat{\boldsymbol{u}}_m \\ \hat{\boldsymbol{v}}_m \\ \hat{\boldsymbol{w}}_m \end{bmatrix} = \boldsymbol{R}_{\boldsymbol{xyz_m}} \cdot \begin{bmatrix} \hat{\boldsymbol{x}}_1 \\ \hat{\boldsymbol{y}}_1 \\ \hat{\boldsymbol{z}}_1 \end{bmatrix}. \tag{39}$$

The transformation matrix $\boldsymbol{R}_{\boldsymbol{xyz_m}}$ can be expressed as

$$\boldsymbol{R}_{\boldsymbol{xyz_m}} = \begin{bmatrix} \hat{\boldsymbol{u}}_m \\ \hat{\boldsymbol{v}}_m \\ \hat{\boldsymbol{w}}_m \end{bmatrix} \cdot \begin{bmatrix} \hat{\boldsymbol{x}}_1 \\ \hat{\boldsymbol{y}}_1 \\ \hat{\boldsymbol{z}}_1 \end{bmatrix}^{-1}. \tag{40}$$

Since the axial directions of $x_1y_1z_1$ and $x_my_mz_m$ can be determined by Eqs. (35) and (36), and the axial directions of $u_mv_mw_m$ can be obtained by Eq. (37) further, we can obtain the transformation matrix $\boldsymbol{R}_{\boldsymbol{xyz_m}}$ by Eq. (40). By combining Eqs. (38) and (40), we obtain the solutions of the three Euler angles as follows:

$$\xi_{ym} = -\arcsin\left(\boldsymbol{R}_{\boldsymbol{xyz_m}}(1,3)\right), \tag{41}$$

$$\xi_{xm} = \arcsin\left[\frac{\boldsymbol{R}_{\boldsymbol{xyz_m}}(2,3)}{\cos\xi_{ym}}\right], \tag{42}$$

$$\xi_{zm} = \arcsin\left[\frac{\boldsymbol{R}_{\boldsymbol{xyz_m}}(1,2)}{\cos\xi_{ym}}\right]. \tag{43}$$

In theory, the limits of Euler angles are $[-\pi,\pi]$. The yaw angle ξ_{zm} is the rotation angle around the normal line to the imaging plane, and essentially it is the integration angle used to obtain the required cross range resolution. The pitch angle ξ_{ym} and roll angle ξ_{xm} are the rotation angles around the range axis and cross range axis respectively, and they are the spatial-variant angles that reflect the spatial-variant properties of the imaging plane. As is well known, when the integration rotation angle is big, the migration through the resolution cell may occur in the bistatic ISAR, which will affect the imaging quality. So in actual imaging, to ensure the imaging quality, the integration rotation angle is generally not more than $6^\circ\sim7^\circ$. Thus, in the general case, the Euler angles are small, and the limit $[-\pi/18,\pi/18]$ is sufficient to meet the need. Note that

the limit has no effect on the subsequent data processing.

The coordinates of scatter P_1 are (x_p, y_p, z_p) in the $x_1y_1z_1$ system, and the coordinates of scatter P_m are (u_{pm}, v_{pm}, w_{pm}) in the $u_mv_mw_m$ system, which satisfy the following equation.:

$$\left[\begin{array}{ccc} u_{pm} & v_{pm} & w_{pm} \end{array}\right] \cdot \left[\begin{array}{c} \hat{\boldsymbol{u}}_m \\ \hat{\boldsymbol{v}}_m \\ \hat{\boldsymbol{w}}_m \end{array}\right] = \left[\begin{array}{ccc} x_p & y_p & z_p \end{array}\right] \cdot \left[\begin{array}{c} \hat{\boldsymbol{x}}_1 \\ \hat{\boldsymbol{y}}_1 \\ \hat{\boldsymbol{z}}_1 \end{array}\right]. \quad (44)$$

Combining Eqs. (39) and (44), we can obtain the coordinates of scatter P_m as

$$\left[\begin{array}{ccc} u_{pm} & v_{pm} & w_{pm} \end{array}\right] = \left[\begin{array}{ccc} x_p & y_p & z_p \end{array}\right] \cdot \boldsymbol{R}^{-1}_{\boldsymbol{xyz_m}}. \quad (45)$$

Since $\boldsymbol{R}_{\boldsymbol{xyz_m}}$ is a unit orthogonal matrix, the inverse of $\boldsymbol{R}_{\boldsymbol{xyz_m}}$ is its transpose matrix, i.e. $\boldsymbol{R}^{-1}_{\boldsymbol{xyz_m}} = \boldsymbol{R}^{\mathrm{T}}_{\boldsymbol{xyz_m}}$. Equation (45) can be rewritten as

$$\left[\begin{array}{ccc} u_{pm} & v_{pm} & w_{pm} \end{array}\right]^{\mathrm{T}} = \boldsymbol{R}_{\boldsymbol{xyz_m}} \cdot \left[\begin{array}{ccc} x_p & y_p & z_p \end{array}\right]^{\mathrm{T}}. \quad (46)$$

By using Eq. (46), we can obtain the position histories of scatter P projected onto the imaging plane during imaging.

4.2. Analysis of the effect of spatial-variant property on image quality

Assuming that the two radars are ideally synchronous, and the transmitter emits a chirp signal with a period of T_{PRT}, we have

$$s_t(\hat{t}, t_m) = \mathrm{rect}\left(\frac{\hat{t}}{T_{\mathrm{p}}}\right) \exp\left\{\mathrm{j}2\pi(f_{\mathrm{c}}t + \frac{1}{2}\mu\hat{t}^2)\right\}, \quad (47)$$

where $\mathrm{rect}(u)$ is the rectangular window function defined as $\mathrm{rect}(u) = 1$ if $|u| \le 0.5$ and $\mathrm{rect}(u) = 0$ otherwise; $\hat{t}$ is the fast time; $t_m = mT_{\mathrm{PRT}}$, $(m = 0, 1, 2, \ldots)$ is the transmitting time, named slow time; t is the total time and $\hat{t} = t - t_m$; T_{p} is the pulse width; f_{c} is the carrier frequency; μ is the chirp rate.

At the time t_m, let ΔR_{pm} be the difference between the sum of the distance from scatter P_m to two radars (transmitter and receiver) and the sum of the distance from the center of the target to two radars. We can obtain the range profile of scatter P_m through pulse compression. Then the range profile after ideal motion compensation can be written as[8,18]

$$\begin{aligned} s_{\mathrm{c}}(\hat{t}, t_m) &= A_p \cdot \mathrm{sinc}\left[\mu T_p\left(\hat{t} - \frac{\Delta R_{pm}}{c}\right)\right] \\ &\quad \times \exp\left(-\mathrm{j}2\pi f_{\mathrm{c}}\frac{\Delta R_{pm}}{c}\right), \end{aligned} \quad (48)$$

where A_{p} is the signal amplitude, and c is the speed of light in free space. From Eq. (48), the peak position of the range profile occurs at the time $\hat{t} = \Delta R_{pm}/c$. The Doppler frequency can be expressed as

$$f_{\mathrm{d}} = \frac{f_{\mathrm{c}}}{c} \cdot \frac{\mathrm{d}R_{pm}}{\mathrm{d}t_m}$$

obtained from the phase.

In bistatic ISAR, the length of ΔR_{pm} is $2\cos(\beta_m/2)$ times the length of the projection of vector $\boldsymbol{O}_m\boldsymbol{P}_m$ onto the bistatic angle bisector,[19] that is, the value of R_{pm} is $2\cos(\beta_m/2)$ times the coordinate value of scatter P_m onto the range axis in the $u_mv_mw_m$ system. Taking the attitude-stabilized rotation into account, the range axis is the v_m axis, and then the range projection value v_{pm} of scatter P_m onto the range axis can be obtained by Eqs. (38) and (46) as follows:

$$\begin{aligned} v_{pm} &= (-\sin\xi_{zm}\cos\xi_{xm} + \cos\xi_{zm}\sin\xi_{ym}\sin\xi_{xm})x_{\mathrm{p}} \\ &\quad + (\cos\xi_{zm}\cos\xi_{xm} + \sin\xi_{zm}\sin\xi_{ym}\sin\xi_{xm})y_{\mathrm{p}} \\ &\quad + \cos\xi_{ym}\sin\xi_{xm}z_{\mathrm{p}}. \end{aligned} \quad (49)$$

We can write R_{pm} as

$$\begin{aligned} \Delta R_{pm} &= 2v_{Pm}\cos\frac{\beta_m}{2} \\ &= 2(-\sin\xi_{zm}\cos\xi_{xm} + \cos\xi_{zm}\sin\xi_{ym}\sin\xi_{xm})\cos\frac{\beta_m}{2}x_{\mathrm{p}} \\ &\quad + 2(\cos\xi_{zm}\cos\xi_{xm} + \sin\xi_{zm}\sin\xi_{ym}\sin\xi_{xm})\cos\frac{\beta_m}{2}y_{\mathrm{p}} \\ &\quad + 2\cos\xi_{ym}\sin\xi_{xm}\cos\frac{\beta_m}{2}z_{\mathrm{p}}. \end{aligned} \quad (50)$$

Using Eq. (50), the instantaneous frequency of scatter P_m can be found by taking the slow derivative of the phase in Eq. (48) as follows:

$$\begin{aligned} f_{\mathrm{d}} &= -\frac{1}{2\pi}\cdot\frac{\mathrm{d}}{\mathrm{d}t_m}\left(-2\pi f_{\mathrm{c}}\frac{\Delta R_{pm}}{c}\right) \\ &= \frac{2f_{\mathrm{c}}}{c}\left[\left(-\xi'_{zm}\cos\xi_{zm}\cos\xi_{xm}\cos\frac{\beta_m}{2}\right.\right. \\ &\quad + \xi'_{xm}\sin\xi_{zm}\sin\xi_{xm}\cos\frac{\beta_m}{2} \\ &\quad \left.+ \frac{\beta'_m}{2}\sin\xi_{zm}\cos\xi_{xm}\sin\frac{\beta_m}{2}\right)x_{\mathrm{p}} \\ &\quad + \left(-\xi'_{zm}\sin\xi_{zm}\sin\xi_{ym}\sin\xi_{xm}\cos\frac{\beta_m}{2}\right. \\ &\quad \left.+ \xi'_{ym}\cos\xi_{zm}\cos\xi_{ym}\sin\xi_{xm}\cos\frac{\beta_m}{2}\right)x_{\mathrm{p}} \\ &\quad + \left(\xi'_{xm}\cos\xi_{zm}\sin\xi_{ym}\cos\xi_{xm}\cos\frac{\beta_m}{2}\right. \\ &\quad \left.- \frac{\beta'_m}{2}\cos\xi_{zm}\sin\xi_{ym}\sin\xi_{xm}\sin\frac{\beta_m}{2}\right)x_{\mathrm{p}} \\ &\quad + \left(-\xi'_{zm}\sin\xi_{zm}\cos\xi_{xm}\cos\frac{\beta_m}{2}\right. \\ &\quad - \xi'_{xm}\cos\xi_{zm}\sin\xi_{xm}\cos\frac{\beta_m}{2} \\ &\quad \left.- \frac{\beta'_m}{2}\cos\xi_{zm}\cos\xi_{xm}\sin\frac{\beta_m}{2}\right)y_{\mathrm{p}} \\ &\quad + \left(\xi'_{zm}\cos\xi_{zm}\sin\xi_{ym}\sin\xi_{xm}\cos\frac{\beta_m}{2}\right. \\ &\quad \left.+ \xi'_{ym}\sin\xi_{zm}\cos\xi_{ym}\sin\xi_{xm}\cos\frac{\beta_m}{2}\right)y_{\mathrm{p}} \\ &\quad + \left(\xi'_{xm}\sin\xi_{zm}\sin\xi_{ym}\cos\xi_{xm}\cos\frac{\beta_m}{2}\right. \end{aligned}$$

$$-\frac{\beta_m'}{2}\sin\xi_{zm}\sin\xi_{ym}\sin\xi_{xm}\sin\frac{\beta_m}{2}\Big)y_{\rm p}$$
$$+\Big(-\xi_{ym}'\sin\xi_{ym}\sin\xi_{xm}\cos\frac{\beta_m}{2}$$
$$+\xi_{xm}'\cos\xi_{ym}\cos\xi_{xm}\cos\frac{\beta_m}{2}$$
$$-\frac{\beta_m'}{2}\cos\xi_{ym}\sin\xi_{xm}\sin\frac{\beta_m}{2}\Big)z_{\rm p}\Big], \quad (51)$$

where $\xi' = {\rm d}\xi/{\rm d}t_m$ represents the derivative of the slow time. Equations (50) and (51) describe the range histories and Doppler histories during imaging, respectively. When the values of yaw angle ξ_{zm}, pitch angle ξ_{ym}, roll angle ξ_{xm}, and bistatic angle β_m change, the peak positions of range and Doppler frequency also change; it may cause the migration through resolution cells, which may result in image blurring. Thus equations (50) and (51) are the evidences of image quality analysis. For different imaging segments, the Euler angles and bistatic angle have different variation characteristics, and the degrees of migration through resolution cells differ from each other. Then we obtain different quality ISAR images further. So it is necessary to analyze the influence of each angle on image quality, which provides a theoretical guidance for imaging experiment and the selection of imaging segments.

The above two equations are quite complex, especially Eq. (51). Considering that the yaw angle, pitch angle, and roll angle are all very small, the cosine term can be replaced by 1, and their high order sine terms (order greater than or equal to 3) can be ignored. Then equations (50) and (51) can be simplified into

$$\Delta R_{pm} = 2(-\sin\xi_{zm}+\sin\xi_{ym}\sin\xi_{xm})\cos\frac{\beta_m}{2}x_{\rm p}$$
$$+2\cos\frac{\beta_m}{2}y_{\rm p}+2\sin\xi_{xm}\cos\frac{\beta_m}{2}z_{\rm p}, \quad (52)$$
$$f_{\rm d} = \frac{2f_{\rm c}}{c}\Big[\Big(-\xi_{zm}'\cos\frac{\beta_m}{2}+\frac{\beta_m'}{2}\sin\xi_{zm}\sin\frac{\beta_m}{2}$$
$$+\xi_{ym}'\sin\xi_{xm}\cos\frac{\beta_m}{2}+\xi_{xm}'\sin\xi_{ym}\cos\frac{\beta_m}{2}\Big)x_{\rm p}$$
$$+\Big(-\xi_{zm}'\sin\xi_{zm}\cos\frac{\beta_m}{2}$$
$$-\xi_{xm}'\sin\xi_{xm}\cos\frac{\beta_m}{2}-\frac{\beta_m'}{2}\sin\frac{\beta_m}{2}\Big)y_{\rm p}$$
$$+\Big(\xi_{xm}'\cos\frac{\beta_m}{2}-\frac{\beta_m'}{2}\sin\xi_{xm}\sin\frac{\beta_m}{2}\Big)z_{\rm p}\Big]. \quad (53)$$

Both equations can be written as the superposition of non-spatial-variant terms and spatial-variant additional terms, i.e.,

$$\Delta R_{pm} = \Delta R_{pm_z}+\Delta R_{pm_xy}, \quad (54)$$
$$f_{\rm d} = f_{\rm d_z}+f_{\rm d_xy}, \quad (55)$$

where

$$R_{pm_z} = -2\sin\xi_{zm}\cos\frac{\beta_m}{2}x_{\rm p}+2\cos\frac{\beta_m}{2}y_{\rm p}, \quad (56)$$
$$R_{pm_xy} = 2\sin\xi_{ym}\sin\xi_{xm}\cos\frac{\beta_m}{2}x_{\rm p}+2\sin\xi_{xm}\cos\frac{\beta_m}{2}z_{\rm p}, \quad (57)$$
$$f_{\rm d_z} = \frac{2f_{\rm c}}{c}\Big[\Big(-\xi_{zm}'\cos\frac{\beta_m}{2}+\frac{\beta_m'}{2}\sin\xi_{zm}\sin\frac{\beta_m}{2}\Big)x_{\rm p}$$
$$+\Big(-\xi_{zm}'\sin\xi_{zm}\cos\frac{\beta_m}{2}-\frac{\beta_m'}{2}\sin\frac{\beta_m}{2}\Big)y_{\rm p}\Big], \quad (58)$$
$$f_{\rm d_xy} = \frac{2f_{\rm c}}{c}\Big[\Big(\xi_{ym}'\sin\xi_{xm}\cos\frac{\beta_m}{2}+\xi_{xm}'\sin\xi_{ym}\cos\frac{\beta_m}{2}\Big)x_{\rm p}$$
$$-\xi_{xm}'\sin\xi_{xm}\cos\frac{\beta_m}{2}y_{\rm p}$$
$$+\Big(\xi_{xm}'\cos\frac{\beta_m}{2}-\frac{\beta_m'}{2}\sin\xi_{xm}\sin\frac{\beta_m}{2}\Big)z_{\rm p}\Big], \quad (59)$$

where ΔR_{pm_z} and $f_{\rm d_z}$ are the range information and Doppler information of scatter when the imaging plane has no spatial-variant property, and R_{pm_xy} and $f_{\rm d_xy}$ are the range terms and Doppler terms caused by the spatial-variant imaging plane. When analyzing the effect of the spatial-variant property on imaging, we only need to analyze Eqs. (57) and (59).

The spatial-variant property of bistatic ISAR is concerned with the target motion trajectory and the positions of transmitter and receiver. When the spatial-variant property is serious, the phenomenon of migration through resolution cells occurs, which may result in image blurring. The analysis of the spatial-variant property provides evidence for imaging experiment and the selection of imaging segments.

5. Simulation results

To verify the analysis in this paper, the simulation experiments are performed in this section.

5.1. Simulation scenario

We select the Tiangong-1 satellite as the simulation target, and its six orbital elements are provided by the Space Surveillance Network (SSN) of America in the form of a two-line element (TLE) listed as follows:

1 37820U 11053A 14104.86088755 0.00057267 00000-0 50311-3 0 9357

2 37820 042.7734 335.3498 0012276 284.0961 185.9363 15.67862963146089

The epoch time of initial orbital elements is on 14 April 2014 at 20:39:41. The six orbital elements can be derived from the TLE. Then we can simulate the motion of a satellite in orbit according to the model built in Section 2. Placing the transmitting station in city A, and placing the receiving station in city B, from 05:39:30 to 05:47:50, i.e., in a total time of 500 s the satellite was visible by using the transmitter and receiver. The simulation scenario is shown in Fig. 5, where the solid curve represents the satellite orbit, the diamond denotes a transmitter and the circle refers to a receiver, and the star is the geocentric position. The coordinate system is the Earth-fixed system.

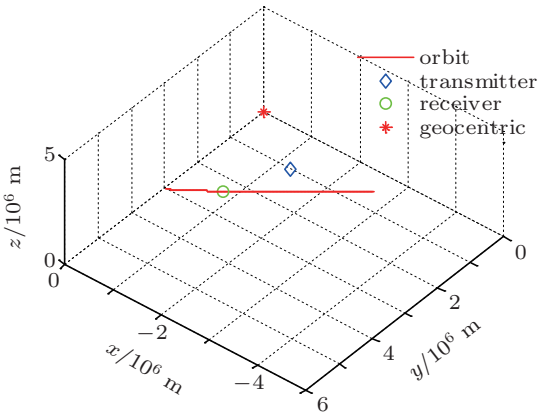


Fig. 5. (color online) Simulation scenario.

5.2. Simulation of spatial-variant angle of imaging plane

To describe the spatial-variant property of the imaging plane intuitively, we simulate the yaw angle, pitch angle, and roll angle curves in steps of 10 s, the results of which are shown in Fig. 6. In the figure, the yaw angle (i.e., integration angle) and pitch angle change greatly but the roll angle has a small variation.

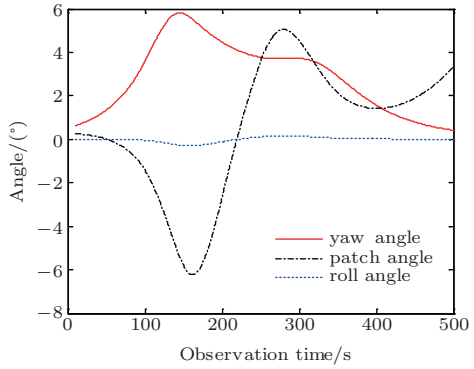


Fig. 6. (color online) Spatial-variant angle curves every 10 s.

The purpose of spatial-variant analysis is to analyze the effect of a changing imaging plane on image quality. The range terms and Doppler terms caused by the spatial-variant imaging plane are shown in Eqs. (57) and (59), where range terms ΔR_{pm_xy} contain two factors and Doppler terms f_{d_xy} contain five factors. These seven factors can be written as follows:

$$\text{Range factor 1, } \Delta R_{pm_xy1} = 2\sin\xi_{ym}\sin\xi_{xm}\cos\frac{\beta_m}{2}x_{\mathrm{p}},$$

$$\text{Range factor 2, } \Delta R_{pm_xy2} = 2\sin\xi_{xm}\cos\frac{\beta_m}{2}z_{\mathrm{p}},$$

$$\text{Doppler factor 1, } f_{\mathrm{d}_xy1} = \frac{2f_{\mathrm{c}}}{c}\xi'_{ym}\sin\xi_{xm}\cos\frac{\beta_m}{2}x_{\mathrm{p}},$$

$$\text{Doppler factor 2, } f_{\mathrm{d}_xy2} = \frac{2f_{\mathrm{c}}}{c}\xi'_{xm}\sin\xi_{ym}\cos\frac{\beta_m}{2}x_{\mathrm{p}},$$

$$\text{Doppler factor 3, } f_{\mathrm{d}_xy3} = -\frac{2f_{\mathrm{c}}}{c}\xi'_{xm}\sin\xi_{xm}\cos\frac{\beta_m}{2}y_{\mathrm{p}},$$

$$\text{Doppler factor 4, } f_{\mathrm{d}_xy4} = \frac{2f_{\mathrm{c}}}{c}\xi'_{xm}\cos\frac{\beta_m}{2}z_{\mathrm{p}},$$

$$\text{Doppler factor 5, } f_{\mathrm{d}_xy5} = -\frac{f_{\mathrm{c}}}{c}\beta'_m\sin\xi_{xm}\sin\frac{\beta_m}{2}z_{\mathrm{p}}.$$

These factors reflect the degree of migration through range and Doppler cells. Let the size of target be 10 m, i.e., $x_{\mathrm{p}} = y_{\mathrm{p}} = z_{\mathrm{p}} = 10$ m, then we will simulate the possible numbers of migration through the range and Doppler cell by the above seven factors also in steps of 10 s. The results are shown in Fig. 7. Figure 7(a) shows the variations of the number of range cell migrations with observation time, and figure 7(b) displays variations of the number of Doppler cell migrations with observation time. We can see that the migration through range cell number is less than 0.25 for a target of this size. However, the Doppler cell number that the migration goes through is greater than 4 at some orbital segments. In addition, it is caused mainly by Doppler factor 4. Doppler factor 4 is a function of the roll angle and height coordinate of scatter. If the scatter has the larger height coordinate, more serious Doppler cell migrations will take place. Therefore, for some imaging segments, the spatial-variant property will deteriorate the image quality. Since the existing correction algorithm[20] cannot correct the Doppler migration caused by the spatial-variant imaging plane, to obtain a high-quality ISAR image, we need to avoid the orbital segments which have a serious spatial-variant property in actual imaging.

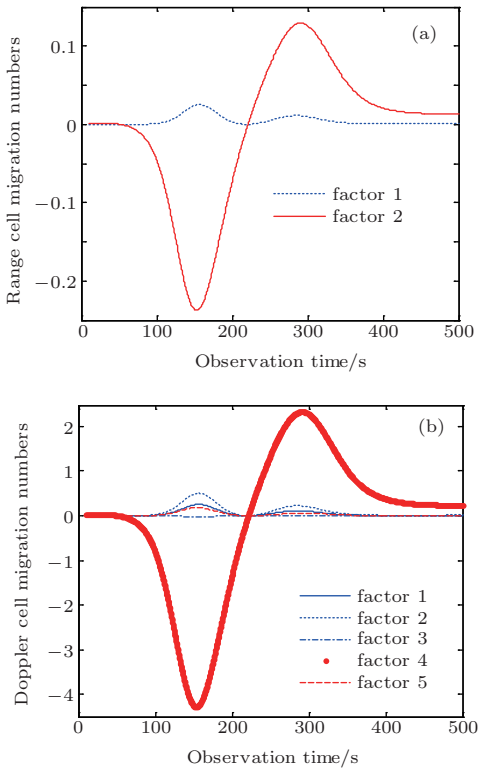


Fig. 7. (color online) The numbers of migrations through range and Doppler cell caused by spatial-variant imaging plane versus observation time: (a) range cell migration numbers; (b) Doppler cell migration numbers.

5.3. Bistatic ISAR imaging simulation

From the above simulation, we can see that the spatial-variant property has little effect on migration through range cell, but has great Doppler migration. To verify the above analysis, the imaging simulations are carried out.

Two different imaging segments are selected for the bistatic ISAR imaging simulation. The observation time for imaging segment 1 is from 145 s to 155 s. The spatial-variant property is serious and it will cause the great image change of different height scatters in theory. The observation time for imaging segment 2 is from 215 s to 225 s. The imaging plane is quite stable with respect to segment 1, and the imaging results of discrete scatters at different heights should be basically the same. The simulation scatter model is shown in Fig. 8, and the coordinate values of 9 scatters are listed in Table 1. The values of range and cross range are as small as 3 m, but the height difference is large, the height coordinate values of scatters $A \sim C$ are 0 m, scatters $D \sim F$ are 15 m, and scatters $G \sim I$ are 30 m. The simulation radar parameters and imaging parameters of two imaging segments are listed in Table 2.

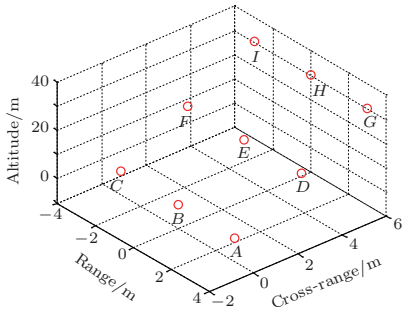


Fig. 8. (color online) Scatter model.

Table 1. Coordinate values of scatters.

	A	*B*	*C*	*D*	*E*	*F*	*G*	*H*	*I*
Range/m	3	0	–3	3	0	–3	3	0	–3
Cross-range/m	0	0	0	3	3	3	6	6	6
Altitude/m	0	0	0	15	15	15	30	30	30

Table 2. Simulation radar parameters and imaging parameters of bistatic ISAR.

Parameter name	Parameter value	Parameter name	Parameter value	Parameter name	Parameter value	
					Imaging segment 1	Imaging segment 2
Carrier frequency	10 GHz	PRF	50 Hz	mean bistatic angle	90.78°	114.03°
Bandwidth	1 GHz	integration pulses	500	integration rotation angle	5.68°	4.02°
Pulse width	20 μms	integration time	10 s	range resolution	0.214 m	0.276 m
Sampling rate	1.25 GHz	imaging algorithm	RD coherent imaging	cross range resolution	0.215 m	0.393 m

The imaging results are shown in Fig. 9. As we can see in Fig. 9(a), the difference of imaging results is quite significant for different height scatters: the higher the scatters, the worse the imaging results are. The scatters in Fig. 9(b) have the same qualities. The reason for the difference between the two figures is that the spatial-variant property is serious in segment 1, which results in migration through Doppler cells of the higher scatters. Note that the image in Fig. 9(a) is askew with respect to the scatter model, which is the image distortion caused by the time-varying bistatic angle.[15]

To quantitatively analyze the effect of height on migration through Doppler cells, the range cell where scatters *B*, *E*, and *H* stay, is extracted. The cross range results of two imaging segments are shown in Fig. 10. The difference in amplitude among the three scatters is large in segment 1, and the scatters *E* and *H* have serious mainlobe expansion. The scatters in segment 2 change a little.

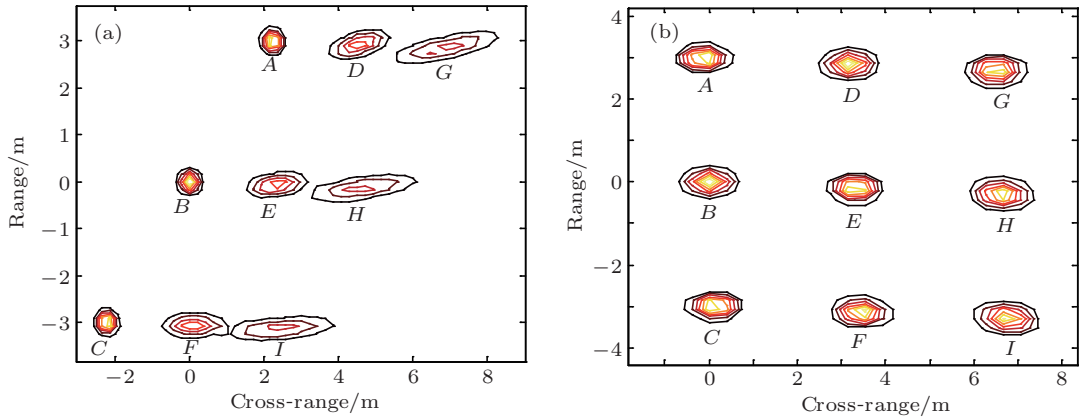


Fig. 9. (color online) Imaging results of two segments: (a) segment 1; (b) segment 2.

We calculate the range and cross range 3-dB mainlobe widths of scatters at different heights of the two imaging segments, and list the results in Table 3. In segment 1, the range 3-dB mainlobe widths of different scatters changes a little, but the cross range 3-dB mainlobe width occupies 1, 6, and 12 cross range cells when the heights are 0, 15, and 30 m. Compared with the result in Fig. 7(b), the scatter at the height of 30 m will cause about 12 Doppler cells to migrate, the imaging

results of bistatic ISAR perfectly match the results in Fig. 7(b). The above results indicate the correctness of the analysis of the spatial-variant property. In segment 2, the range and cross range 3-dB mainlobe widths of different scatters are nearly the same. The results also confirm the conclusion shown in Fig. 7.

Table 3. Statistical results of 3-dB mainlobe width.

	3-dB mainlobe width of range bin/m		3-dB mainlobe width of cross-range bin/m	
	Segment 1	Segment 2	Segment 1	Segment 2
Altitude 0 m (A,B,C)	0.219	0.285 m	0.220	0.405
Altitude 15 m (D,E,F)	0.239	0.285 m	1.257	0.417
Altitude 30 m (G,H,I)	0.252	0.287 m	2.553	0.417

From the comparison between spatial-variant angle and bistatic ISAR imaging results, the actual imaging results are quite consistent with the theoretical analysis, which shows the correctness of the research on the spatial-variant property.

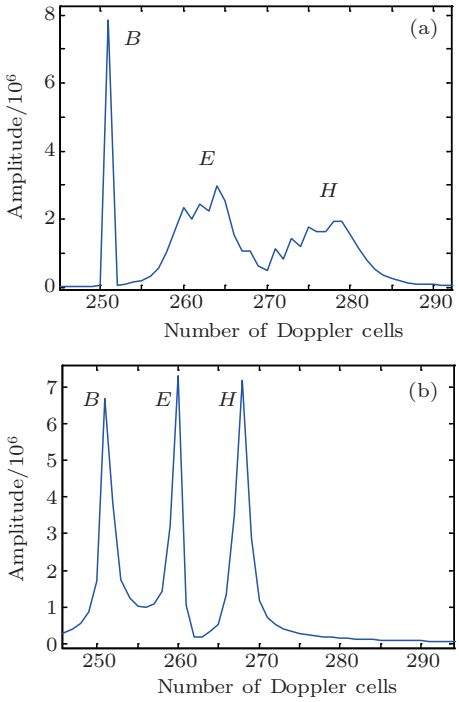


Fig. 10. (color online) Comparisons of cross section between scatters at different heights: (a) segment 1 and (b) segment 2.

6. Conclusions

In an ISAR system, the spatial-variant property of the imaging plane may affect the image quality. The spatial-variant property of the imaging plane of a space target is investigated in this paper. First, the target motion in orbit is simulated based on a two-body model. Second, the instantaneous imaging plane is determined by the vector analysis method. Then three Euler angles are introduced to describe the spatial-variant property of the imaging plane, and the effect of the spatial-variant property on the image quality is analyzed. Finally, the simulation and quantitative analysis are carried out. The results indicate the correctness of spatial-variant property analysis. The research in this paper is of great significance for the selection of imaging segment, and provides evidences for further work in data processing and compensation algorithm. Although the analysis of the spatial-variant property of the bistatic ISAR imaging plane is accomplished in this paper, further research on the correction algorithm of migration through resolution cells is needed.

Appendix A: Derivation of the coordinate representation for transformation matrix

Without loss of generality we derive the coordinate representation that any point $\boldsymbol{M}(M_x,M_y,M_z)$ in space rotates around the rotation axis unit vector $\boldsymbol{A}(A_x,A_y,A_z)$ through an angle η as illustrated in Fig. A1. Let the new point after rotation be $\boldsymbol{M}'\left(M'_x,M'_y,M'_z\right)$.

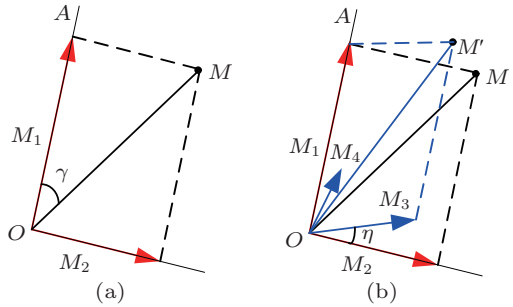


Fig. A1. (color online) Schematic diagram of any point rotating around the rotation axis.

Decompose M into M_1 and M_2, where M_1 is the component parallel to rotation axis A and M_2 is the component perpendicular to A as shown in Fig. A1(a), and let point O be the origin of the coordinate system in space, then the following equations will be obtained:

$$\boldsymbol{M} = \boldsymbol{M}_1 + \boldsymbol{M}_2, \tag{A1}$$

$$\boldsymbol{M}_1 = (\boldsymbol{A}\cdot\boldsymbol{M})\,\boldsymbol{A}, \tag{A2}$$

$$\boldsymbol{M}_2 = \boldsymbol{M} - (\boldsymbol{A}\cdot\boldsymbol{M})\,\boldsymbol{A}. \tag{A3}$$

Rotating $\boldsymbol{M}$ around axis $\boldsymbol{A}$ through an angle η results in $\boldsymbol{M}'$. Let the positive sign of η represent the counterclockwise direction. The parallel component $\boldsymbol{M}_1$ is constant during the rotation and the perpendicular component $\boldsymbol{M}_2$ becomes $\boldsymbol{M}_3$ as shown in Fig. A1(b). Thus

$$\boldsymbol{M}' = \boldsymbol{M}_1 + \boldsymbol{M}_3. \tag{A4}$$

Since the rotation of $\boldsymbol{M}_2$ to $\boldsymbol{M}_3$ is in the plane perpendicular to axis $\boldsymbol{A}$, $\boldsymbol{M}_3$ can be decomposed into $\boldsymbol{M}_2$ and $\boldsymbol{M}_4$, where vector $\boldsymbol{M}_4$ is obtained by counterclockwise rotating $\boldsymbol{M}_2$ through 90°. Let the angle between vector $\boldsymbol{M}$ and rotation axis $\boldsymbol{A}$ be γ, then the amplitude of $\boldsymbol{M}_2$ will be obtained by

$$|\boldsymbol{M}_2| = |\boldsymbol{M}|\sin\gamma. \tag{A5}$$

$\boldsymbol{M}_4$ satisfies the following equations:

$$\boldsymbol{M}_4 = \boldsymbol{A}\times\boldsymbol{M}, \tag{A6}$$

$$|M_4| = |A||M|\sin\gamma. \tag{A7}$$

Since A is a unit vector, by Eqs. (A4) and (A7) we can obtain that the amplitude of M_2 is equal to M_4, i.e., $|M_4| = |M_2|$.

Let M_2' and M_4' be the components of M_3 projected on M_2 and M_4 directions respectively, then

$$M_3 = M_2' + M_4' \tag{A8}$$

with

$$M_2' = |M_3|\cos\eta\frac{M_2}{|M_2|}, \tag{A9}$$

$$M_4' = |M_3|\cos\eta\frac{M_4}{|M_4|}. \tag{A10}$$

Because the amplitude of M_2 is equal to M_3, the amplitudes of M_2, M_3, and M_4 are the same. Equations (A9) and (A10) become

$$M_2' = M_2\cos\eta, \tag{A11}$$

$$M_4' = M_4\cos\eta. \tag{A12}$$

Then equation (A4) can be written as

$$\begin{aligned} M' &= M_1 + M_3 \\ &= M_1 + M_2' + M_4' \\ &= M_1 + M_2\cos\eta + M_4\sin\eta \\ &= (A\cdot M)A + (M - (A\cdot M)A)\cos\eta \\ &\quad + (A\times M)\sin\eta. \end{aligned} \tag{A13}$$

Equation (A13) can be simplified into

$$\begin{aligned} M' = M\cos\eta + (A\cdot M)A(1-\cos\eta) \\ + (A\times M)\sin\eta. \end{aligned} \tag{A14}$$

Each term in Eq. (A14) can be written in the form of a matrix, then

$$M\cos\eta = [M_x, M_y, M_z]\begin{bmatrix} \cos\eta & 0 & 0 \\ 0 & \cos\eta & 0 \\ 0 & 0 & \cos\eta \end{bmatrix}, \tag{A15}$$

$$\begin{aligned} &(A\cdot M)A(1-\cos\eta) \\ &= (1-\cos\eta)(A_xM_x + A_yM_y + A_zM_z)(A_x, A_y, A_z) \\ &= [M_x, M_y, M_z]\cdot\begin{bmatrix} A_x^2 & A_xA_y & A_xA_z \\ A_xA_y & A_y^2 & A_yA_z \\ A_xA_z & A_yA_z & A_z^2 \end{bmatrix}(1-\cos\eta), \end{aligned} \tag{A16}$$

$$\begin{aligned} &(A\times M)\sin\eta \\ &= (A_yM_z - A_zM_y, A_zM_x - A_xM_z, A_xM_y - A_yM_x)\sin\eta \\ &= [M_x, M_y, M_z]\begin{bmatrix} 0 & A_z\sin\eta & -A_y\sin\eta \\ -A_z\sin\eta & 0 & A_x\sin\eta \\ A_y\sin\eta & -A_x\sin\eta & 0 \end{bmatrix}. \end{aligned} \tag{A17}$$

Substituting Eqs. (A15)–(A17) into Eq. (A14) yields

$$M' = [M_x', M_y', M_z'] = [M_x, M_y, M_z]\cdot R_S(\eta), \tag{A18}$$

where $R_S(\eta)$ is the transformation matrix as given below.

$$R_S(\eta) = \begin{bmatrix} A_x^2(1-\cos\eta)+\cos\eta & A_xA_y(1-\cos\eta)+A_z\sin\eta & A_xA_z(1-\cos\eta)-A_y\sin\eta \\ A_xA_y(1-\cos\eta)-A_z\sin\eta & A_y^2(1-\cos\eta)+\cos\eta & A_yA_z(1-\cos\eta)+A_x\sin\eta \\ A_xA_z(1-\cos\eta)+A_y\sin\eta & A_yA_z(1-\cos\eta)-A_x\sin\eta & A_z^2(1-\cos\eta)+\cos\eta \end{bmatrix}. \tag{A19}$$

References

[1] Yang Z Q, Zhang Y S and Luo Y J 1998 *Bistatic (Multistatic) Radar System* (Beijing: Defense Industry Press) pp. 14–15
[2] Ji W J and Tong C M 2013 *Chin. Phys. B* **22** 020301
[3] Zhang Y M, Wang Y H and Zhao C F 2010 *Chin. Phys. B* **19** 084103
[4] Peng S B, Xu J, Meng C Z, Yang J and Peng Y N 2013 *IET International Radar Conference*, April 14–16, Xi'an, China, p. 1
[5] Pan X Y, Wang W, Feng D J, Liu Y C, Fu Q X and Wang G Y 2014 *IET Radar, Sonar Navig.* **8** 173
[6] Ma C Z, TAT SOON YEO, Guo Q and Wei P J 2012 *IEEE Trans. Geosci. Remote Sens.* **50** 3859
[7] Ma C, Gu H, Su W M and Li C Z 2014 *Acta Phys. Sin.* **63** 028403 (in Chinese)
[8] Bai X R, Zhou F and Bao Z 2014 *IEEE Trans. Geosci. Remote Sens.* **52** 2369
[9] Yin J F, Li J D, Wang A M and Li Z 2013 *J. Astronautics* **34** 237
[10] Bai X R, Zhou F, Xing M D and Bao Z 2010 *IEEE Trans. Geosci. Remote Sens. Lett.* **7** 430
[11] Fabrice C, Ali K and Alexandre B 2006 *IEEE Trans. Antennas Propag.* **54** 3529
[12] Deng D H, Zhang Q and Luo Y 2013 *J. Radar* **6** 1
[13] Martorella M, Palmer J and Homer J 2007 *IEEE Trans. Aerosp. Electron. Syst.* **43** 1125
[14] Martorella M, Cataldo D and Brisken S 2013 *IEEE Radar Conference*, April 19–May 3, Ottawa, Ontario, Canada
[15] Dong J, Shang C X and Gao M G 2012 *J. Electron. Inf. Tech.* **32** 1855
[16] Ovliver Montenbruck and Eberhard Gill 2001 *Satellite Orbits: Models, Methods and Applications* (New York: Springer) pp. 157–168
[17] Howard D Curitis, Zhou J H, Xu B and Feng Q S 2009 *Orbit Mechanics* (Beijing, Science Press) pp. 120–203, 25–32
[18] Bao Z, Xing M D and Wang T 2010 *Radar Imaging Technology* (Beijing: Publishing House of Electronics Industry) pp. 243–254
[19] Martorella M 2012 *IEEE Trans. Aerosp. Electron. Syst.* **47** 2673
[20] Huang Y J 2008 *M S Dissertation* (Changsha: National University of Defense Technology)